WANG, S., FAN, Y., YU, C., JIN, S., FERNANDEZ, C. and STROE, D.-I. 2022. Improved covariance matching-electrical equivalent modeling for accurate internal state characterization of packing lithium-ion batteries. *International journal of energy research* [online], 46(3), pages 3602-3620. Available from: https://doi.org/10.1002/er.7408

Improved covariance matching-electrical equivalent modeling for accurate internal state characterization of packing lithium-ion batteries.

WANG, S., FAN, Y., YU, C., JIN, S., FERNANDEZ, C. and STROE, D.-I.

2022

INTERNATIONAL JOURNAL OF
ENERGY RESEARCH

Improved covariance matching - electrical equivalent modeling for accurate internal state characterization of packing lithium-ion batteries

Journal:	*International Journal of Energy Research*
Manuscript ID	ER-21-21370.R2
Wiley - Manuscript type:	Research Article
Date Submitted by the Author:	06-Oct-2021
Complete List of Authors:	wang, shunli; Southwest University of Science and Technology, School of Information Engineering Fan, Yongcun; Southwest University of Science and Technology, School of Information Engineering Yu, Chunmei; Southwest University of Science and Technology, School of Information Engineering Jin, Siyu; Aalborg University Fernandez, Carlos; Robert Gordon University Stroe, Daniel; Aalborg University, Energy Technology
Keywords:	packing lithium-ion batteries, electrical equivalent circuit modeling, cell-to-cell variation, state of balance, adaptive covariance matching, weighting factor correction

Improved covariance matching - electrical equivalent modeling for accurate internal state characterization of packing lithium-ion batteries

Shunli Wang[1], Yongcun Fan[1], Chunmei Yu[1], Siyu Jin[2], Carlos Fernandez[3], Daniel-Ioan Stroe[2]

[1]School of Information Engineering & Robot Technology Used for Special Environment Key Laboratory of Sichuan Province, Southwest University of Science and Technology, Mianyang 621010, China. [2] *Department of Energy Technology, Aalborg University, Pontoppidanstraede 111 9220 Aalborg East, Denmark.* [3]School of Pharmacy and Life Sciences, Robert Gordon University, Aberdeen AB10-7GJ, UK.

Abstract: As for the cell-to-cell inconsistency of packing lithium-ion batteries, accurate equivalent modeling plays a significant role in the working characteristic monitoring and improving the safety protection quality under complex working conditions. In this work, a novel covariance matching - electrical equivalent circuit modeling method is proposed to realize the adaptive working state characterization by considering the internal reaction features, and an improved adaptive weighting factor correction - differential Kalman filtering model is constructed for the iterative calculation process. A new parameter named state-of-balance is introduced to describe the cell-to-cell variation mathematically by forming an effective influence correction strategy. An adaptive covariance matching method is investigated to update and transmit the noise matrix for high-power energy supply conditions, in which the weighting factor correction is conducted by considering the coupling relationship to improve the prediction accuracy. Experimental tests are conducted to verify the estimation effect, in which the closed-circuit voltage responds well corresponding to the battery state variation. The maximum closed-circuit voltage traction error is 1.80% and the maximum SOC estimation error for packing lithium-ion batteries is 1.114% for the long-term experimental tests with the MAE value of 0.00481 and RMSE value of 5.44085E-5. The improved covariance matching - electrical equivalent circuit modeling method provides a theoretical foundation for the reliable application of lithium-ion batteries.

Keywords: packing lithium-ion batteries; electrical equivalent circuit modeling; cell-to-cell variation; state of balance; adaptive covariance matching; weighting factor correction

Corresponding authors: Shunli Wang, wangshunli@swust.edu.cn

1. Introduction

As the energy sustainability determines the vitality of lithium-ion batteries in the power supply application, mathematical modeling is necessary to be conducted to increase the safety level and cycling lifespan of packing lithium-ion batteries and the battery system also benefits from the electrical modeling strategy optimization [1-3]. Constructed by multiple cells, the battery system has characteristics of large capacity, extensive series-parallel nodes, and strict safety boundaries. Meanwhile, effective real-time state monitoring and control become crucial to ensure the safety and durability of the power supply systems [4-10]. In pack applications, balancing and equalization are conducted and the balancing current is usually not measured. In this case, the current is no longer accurate when identifying the model parameters. Consequently, only the cell voltage and closed-circuit voltage (CCV) can be used to compensate for the cell-to-cell difference influence [11]. As a crucial technology of the battery system, the accurate estimation of model parameters and state of charge (SOC) has great significance for the accurate remaining useful life (RUL) prediction [12-15], which optimizes the overall performance of the battery packs.

The battery working process has strong nonlinear dynamic characteristics, involving multiple mutually coupled processing schedules, including electrochemical reaction, energy-heat transformation, and so on. The electrical equivalent circuit (EEC) modeling is investigated to realize the accurate parameter identification as well as the mathematical state-space expression, which becomes a basis of the subsequent safety protection [16-20]. The precise modeling and effective mathematical expression are important for the accurate working state and model parameter estimation in the industrial power supply applications, in which the sensitivity of the working environment situation increases along with the modeling difficulties [21-23]. Considering the aging characteristics and complex environmental variability, it is crucial to take in multiple aspects and establish accurate mathematical models for performance optimization [24, 25]. To simulate the responding voltage characteristics under different power supply conditions, the equivalent modeling is divided into black-box, electrochemical, and electrical circuit types. The black-box modeling is a kind of non-linear treatment to describe the voltage-response characteristics [26-28], which includes neural networks (NN), support vector machines (SVM), and so on. The black-box model is trained by the real-time measured data, depending on the experimental test seriously [29-31]. Subsequently, to describe the dynamic characteristics, improved EEC modeling methods are introduced into the accurate battery state description.

The cell-to-cell consistency difference has a great influence on the packing interaction, in which a complex series-parallel combining structure is used to overcome the limitation of the single battery cell for the special voltage and capacity requirement. The inconsistency between the battery cells makes the packing equivalent modeling treatment to be difficult in the power supply process. Symptoms such as spontaneous combustion, explosion, and early scrap caused by lacking safety management have brought hidden safety hazards and economic losses to society and posed a great threat to the power supply security [32-35]. Therefore, breakthrough modeling is one of the core battery management factors, which is also an effective method to prevent safety accidents. When it is combined with a complex monolithic structure, the packing equivalent modeling is crucial to improve the management efficiency and safety. The noise interference should be conducted under dynamic working conditions and the reliable battery application needs an exact equivalent model to realize the mathematical characterization, which is the decision basis of energy controlling and management [36-39]. As the internal battery parameters in the equivalent model cannot be measured online and need to be calculated indirectly through the experimental analysis, such as ohmic resistance, polarization resistance, and capacitance [40-42]. Therefore, the mathematical description could only be implemented by utilizing external measurable parameters, such as voltage, current, and temperature.

The state-space equation of the EEC model should be established for the iterative calculation, which is then introduced into the battery state evaluation process considering the voltage limitation of the state of power (SOP) prediction. However, ignoring the cell-to-cell difference impacts on the state monitoring and management may result in the over-charge or over-discharge risks [43-46]. As a result, outside model parameters are used as constraints, such as voltage, current, SOC, state-of-health (SOH), and rated capacity. Afterward, the peak SOP is predicted by the resistance-capacitance EEC model, and the model parameters are obtained by the genetic calculation to improve the estimation accuracy, according to which the suitable linearization treatment is conducted for the SOC and SOP co-estimation [21, 47-53]. The statistical analysis is investigated to describe the influencing mechanism of various constraints on the working state and model parameter estimation [54-56], which has an important significance for the energy and power characteristics but adapts to limited scenarios and complex strategies [54-56]. How to estimate the battery state effectively is an important solution to improve the estimation accuracy by conducting the packing equivalent modeling as well as the research on the joint estimation of working state and model parameters.

The coupling relationship between model parameters and state factors is not considered in most existing researches, which has a great effect on the estimation accuracy, such as ohmic resistance, polarization resistance, and capacitance. Consequently, an improved packing covariance matching – electrical equivalent circuit (CM-EEC) modeling method is proposed for the joint estimation of working state and model parameters considering the consistency influences by introducing a new factor of SOB considering the cell voltage difference over internal-connected battery cells under complex working conditions. Through modular circuit characterization, the battery state variation law is obtained along with the complex working conditions. An improved weighting factor correction - differential Kalman filtering (WFC-DKF) model is constructed for the iterative calculation. The adaptive covariance matching treatment is investigated to update and transmit the noise matrix for high-power energy supply conditions, in which the weighting factor correction and coupling relationship are further explored to improve the prediction accuracy. Combined with the influencing factor correction strategy analysis, the inter-unit inconsistency effect is reduced effectively. The proposed modeling and collaborative prediction-correction methods play an important role in improving the battery state estimation accuracy and robustness.

2. Mathematical Analysis

2.1. *Covariance matching - Electrical Equivalent Modeling*

The improved CM-EEC modeling mechanism is revealed to estimate the collaborative battery state effectively for the crucial breakthroughs in energy management. The optimizing strategy is analyzed for different power supply conditions as well as safety protection. The attenuation modeling is conducted together with the coordinated estimation of working state and model parameters to realize the safe and reliable wide-temperature-range energy supply. Moreover, full-life-cycle modeling and dynamic characteristic description are conducted. The online model parameter identification is combined with the SOC estimation, which is also a collaborative premise of the SOH evaluation. Furthermore, the performance description ensures the scientific and advanced nature of the entire theoretical modeling process. The initial implementation and exploratory application are conducted to verify the effectiveness and usability, as shown in Figure 1.

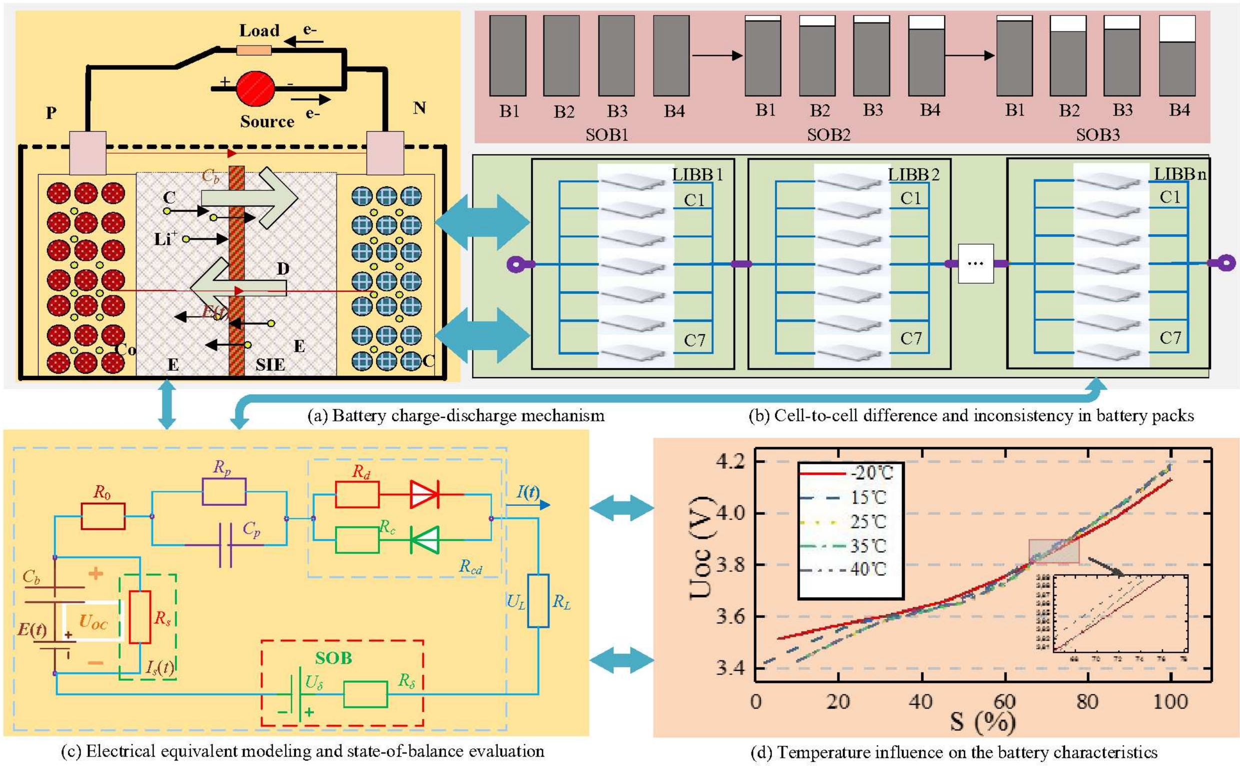

Figure 1. Covariance matching - electrical equivalent circuit modeling for lithium-ion battery packs

In Figure 1, subgraph (a) describes the inner structure and reaction process of the battery cell; subgraph (b) describes the packing connection structure of the inner connected battery cells, in which the cell-to-cell difference is also expressed by introducing the parameter named SOB; subgraph (c) describes the packing equivalent circuit topological structure; subgraph (d) describes the inner parameter relationship corresponding to the temperature and current variation. As can be known from the mathematical analysis, the inner reaction of the battery cell for subgraph (a) and connection structure for cell-to-cell difference expression of subgraph (b) can be used as the basis of the CM-EEC modeling shown in subgraph (c). The core parameter variation law corresponding to the working condition change of subgraph (d) plays an important role in the model construction and parameter identification process. As for the dynamic energy supply randomness in the wide-temperature-range environmental conditions, the input-output characteristics are considered under various conditions to realize the accurate mathematical expression. To improve the crucial whole-life-cycle performance evolution, the CM-EEC modeling is realized for the precise battery working characteristic description as well as the effective feature extraction. The temperature-gradient-change influence on the energy attenuation is anatomized, according to which the correction strategy is investigated that is suitable to the varying ambient temperature levels. And then, the influencing mechanism is obtained together with the crucial factor changing functions.

2.2. *Online Model Parameter Identification*

The online parameter identification is constructed for the improved CM-EEC model to obtain the accurate mathematical expression of the battery working characteristics. The equivalent confirmatory is carried out that is adaptive to various parameter changes with an effective mathematical expression effect. The decreased voltage and the rapid CCV recovery at the initial time point is caused by the ohmic resistance R_0. The gradual voltage decrease is expressed by the resistance-capacitance circuit of the CM-EEC model. Therefore, the ohmic resistance is obtained from segments of AB and CD, as shown in Figure 2.

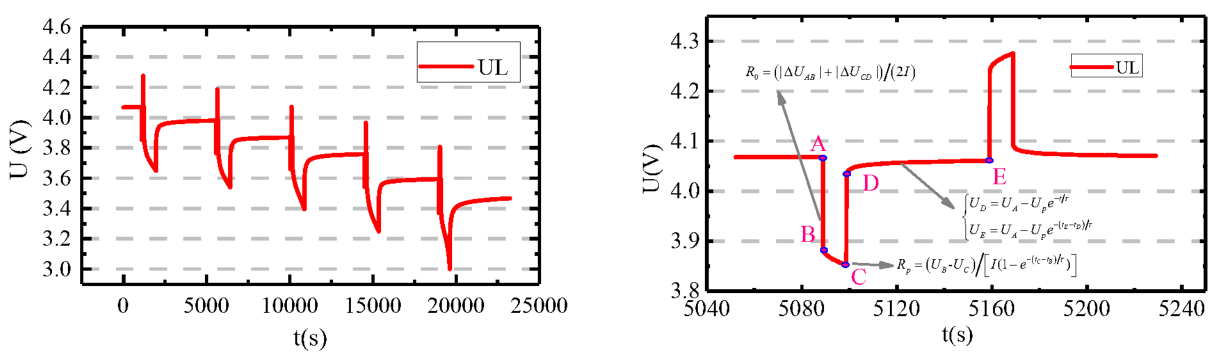

(a) Whole procedure of the pulse power test

(b) Single pulse-current test and its voltage variation

Figure 2. Voltage variation in the pulse power current experimental tests

In Figure 2, the polarization parameter value of the resistance-capacitance circuit is obtained from segments of BC and DE. As can be known from theoretical analysis, the calculation formula of R_0 is obtained, as shown in Equation (1).

$$R_0 = \frac{(|\Delta U_{AB}| + |\Delta U_{CD}|)}{(2I)} \tag{1}$$

In Equation (1), R_0 is the internal resistance. ΔU_{AB} and ΔU_{CD} are the voltage changes varying from time point A to B as well as C to D. According to the parameter influencing results for the SOC estimation, the combined calculation is conducted with highly robust adaptive characteristics as well as the WFC-DKF optimization based on the state-space description, considering the dynamic effect of temperature, aging, and current rate variation. Corresponding to the zero-input response of the CM-EEC model shown in Figure 1, the corresponding segment voltage variation is obtained as shown in Figure 2 (b). Consequently, the mathematical relationship is obtained, as illustrated in Equation (2).

$$\begin{cases} U_D = U_A - U_p e^{-\frac{t}{\tau}} \\ U_E = U_A - U_p e^{-\frac{(t_E - t_D)}{\tau}} \end{cases} \tag{2}$$

In Equation (2), U_D is the CCV value at the time point t_D; U_A is the CCV value at the time point t_A; U_E is the CCV value at the time point t_E; U_p is the polarization voltage; τ is the time constant for the parallel connected RC circuit of R_pC_p. The influencing factor is described under different working conditions based on the CM-EEC modeling, and the mathematical description is utilized by combining the working condition influence to construct different component modules, which is performed along with the structural optimization. The module characterization is realized by combining the CM-EEC model and structural changes, according to which the mathematical characteristic description is conducted adaptive to different working conditions by utilizing the streamlined particles, unscented transformation, and functional modification. Subsequently, adaptive joint model parameters and SOC estimation are conducted. As for the time constant calculation, the mathematical relationship is constructed, as shown in Equation (3).

$$\tau = -\frac{(t_E - t_D)}{ln\left[\frac{(U_A - U_E)}{(U_A - U_D)}\right]} \tag{3}$$

In Equation (3), U_D is the CCV value at the time point t_D; U_A is the CCV value at the time point t_A; U_E is the CCV value at the time point t_E; τ is the time constent. The piece-wise linearization processing is realized for the nonlinear battery system, according to which the adaptive mathematical relationship is obtained between the state-space equation and time-varying model parameters. The exact mathematical characteristic description is investigated to provide a theoretical basis of constructing the adaptive joint SOC and model parameter estimation model, in which R_p is calculated from the voltage variation between the time points of B and C, as shown in Equation (4).

$$R_p = \frac{(U_B - U_C)}{\left[I(1 - e^{-\frac{(t_C - t_B)}{\tau}})\right]} \tag{4}$$

In Equation (4), U_B is the CCV value at the time point t_B; U_C is the CCV value at the time point t_C; R_p is the polarization resistance; τ is the time constant for the parallel connected RC circuit of R_pC_p; I is the current in the pulse charge-discharge test. As the model parameters are obtained at each SOC level, the point-to-point calculation treatment picks up data for the entire pulse power response, which is used sufficiently in the accurate identification process. According to the electrochemical characteristics, several electronic components are used in the state-space equations, including voltage sources, resistors, and capacitors. Combined with the internal resistance and resistance-capacitance network, the improved CM-EEC model is constructed to perform the high-precision battery state estimation, which is then introduced into the improved iterative calculation process, fully considering the circuit response to the SOC variation. The resistance-capacitance circuit determines the output voltage towards the SOC variation, which is realized by combining advantages of electrochemical and electrical description.

As an effective model-based estimation approach, the appropriate CM-EEC modeling method is used to characterize the dynamic behavior of the voltage response to the specific SOC levels. As shown in Figure 1, the resistor-capacitor circuit boosts the modeling accuracy and structural effect. The configuration of the corresponding circuit model is adequate for the time-varying temperature conditions. R_0 is the battery ohmic resistance. R_p and C_p indicate the polarization resistance and capacitance respectively. The open-circuit voltage (OCV) is indicated by U_{OC} which features a monotonous relationship to the SOC variation. I_L is the current and U_L is the CCV. The OCV is reflected by U_1, U_2, and together with the equivalent circuit components respectively, according to which the mathematical relationship is derived, as shown in Equation (5).

$$U_L = U_{OC}(S) - U_1 - U_2 - (R_0 \times I_L) - U_\delta - (R_\delta \times I_L) \tag{5}$$

In Equation (5), $U_{OC}(S)$ is the OCV value corresponding to a particular SOC level; U_1 is polarization voltage for the parallel connected RC circuit of R_pC_p; U_2 is voltage for the parallel connected resistance circuit of $R_c||R_d$; R_0 is the ohmic resistance; I_L is current flowing through the whole circuit; U_δ is the reverse voltage source for the influencing effect of the cell-to-cell difference; R_δ is the added resistance influenced by the cell-to-cell difference effect; U_1, U_2, and are taken as state variables; U_L is the observing vector. Aiming at the dynamic power supply characteristics under wide-temperature-range conditions, the model parameter changing function is obtained along with the variation of the charge-discharge current rate, temperature, and other influencing factors, according to which the modeling equations are derived, as shown in Equation (6).

$$U_1 = (R_p||C_p)I_L; U_2 = (R_c||R_d)I_L; S = 1 - {}^{I_L t}/(\eta Q_n) \tag{6}$$

In Equation (6), U_1 is polarization voltage for the parallel connected RC circuit of R_pC_p; U_2 is the voltage for the parallel connected resistance circuit of $R_c||R_d$; S is the SOC value that can be calculated by the closed-circuit current I_L, the Coulomb efficiency η and rated capacity Q_n. As for the improved CM-EEC modeling, $[S\ U_1\ U_2]$ is set as a state variable matrix, which is then used to describe the battery operating characteristics by the mathematical state-space equation. The parameters in the state-space equation have an obvious relationship towards the working condition change, including the environmental temperature and current. Besides, the main factor variation law also changes in the adaptive correction process to make the iterative calculation have self-learning characteristics, so that the model can be adaptive to the ambient environment change and the aging process. By introducing the adaptive self-learning mechanism, the environmental change is taken into consideration as well as the aging effect. The theoretical analysis is carried out for the online parameter identification, according to which the relationship is obtained between model parameters and influencing factors. Consequently, the state-space equation is obtained for the mathematical description, as shown in Equation (7).

$$\begin{cases} \begin{bmatrix} S_{k+1} \\ U_{1,k+1} \\ U_{2,k+1} \end{bmatrix} = \begin{bmatrix} 1 & 0 & 0 \\ 0 & e^{-t/\tau_p} & 0 \\ 0 & 0 & e^{-t/\tau_c} \end{bmatrix} \begin{bmatrix} S_k \\ U_{1,k} \\ U_{2,k} \end{bmatrix} + \begin{bmatrix} -t/(\eta Q_n) \\ R_p\left(1-e^{-t/\tau}\right) \\ R_2 \end{bmatrix} I(k) \\ U_{k+1} = U_{OC}(S_{k+1}) - U_{1,k+1} - U_{2,k+1} - I(k)R_0 - U_\delta - [R_\delta \times I(k)] \end{cases} \tag{7}$$

In Equation (7), $[S\ U_1\ U_2]$ is the state variable matrix; $k+1$ and k are two adjacent time points; R_p is the polarization resistance; η is the Coulomb efficiency; Q_n is the rated capacity; τ is the time constant for the parallel connected RC circuit of R_pC_p; R_2 is the charge-discharge difference resistance that equals R_c for charging and R_d for discharging; $I(k)$ is the overall current at the time point of k; $U_{OC}(S_{k+1})$ is the OCV value corresponding to the particular SOC level at the time point $k+1$; U_1 is polarization voltage; U_2 is voltage for the parallel connected resistance circuit of $R_c||R_d$; R_0 is the ohmic resistance; U_δ is the reverse voltage source for the influencing effect of the cell-to-cell difference; R_δ is the resistance for the added resistance influenced by the cell-to-cell difference and variation. Combining the variance and coefficient, SOB is introduced to describe the difference between the internal-connected battery cells. The SOB value is then incorporated into the online parameter identification and the iterative calculation process by implementing the mathematical expression, according to which the comprehensive CM-EEC model is established that is adaptive to the whole-life-cycle battery system features. Depending on the variation of the terminal CCV relaxation represented by the first part of Equation (8), the second-order constant parameters are calculated accordingly. Replacing the prediction coefficient factors and updating the calculation process, the mathematical relationship is obtained for the simplified expression of the polarization effect, as shown in Equation (8).

$$\mathrm{U_L} = \mathrm{U_{OC}} - \mathrm{IR_p} e^{\frac{-t}{\tau}} = \mathrm{U_{OC}} - a e^{-bt}, \tau = \mathrm{R_p C_p} \tag{8}$$

In Equation (8), $\mathrm{U_L}$ is CCV and U_{OC} is OCV; I is the current; R_p is the polarization resistance; τ is the time constant for the parallel connected RC circuit of R_pC_p; a and b are coefficient parameters for the exponential function. The online parameter identification is conducted by mathematical modeling, in which the covariance is taken as a known factor together with the noise characteristics. And then, the additional environmental influence is described by sub-modules. After the state-space equation is established, the initial coefficient value is determined, so that the online parameter identification is implemented in a separate module. Aiming at the joint model parameter and SOC estimation, the iterative calculation schedule is constructed. Comparing the coefficients in two sub formulas illustrated in Equation (8), the mathematical calculation relationship for the polarization effect is obtained, as shown in Equation (9).

$$R_p(S) = \frac{a}{I_L}, C_p(S) = \frac{1}{(R_p \times b)} \tag{9}$$

In Equation (9), R_p is the polarization resistance; C_p is the polarization capacitance; I_L is the overall current flowing through the circuit; a and b are coefficient parameters for the exponential function. To obtain the accurate mathematical expression of the battery working characteristics, different internal factors are expressed by using the proposed adaptive CM-EEC model adaptive to the cell-to-cell cascaded structures of the lithium-ion battery packs. Assuming that the voltage before the current change is expressed by U_0 and the varying voltage is described by U_1, the ohmic resistance calculation can be realized, as shown in Equation (10).

$$R_0(S) = \frac{\Delta U}{I_L} = \frac{(U_1 - U_0)}{I_L} \tag{10}$$

In Equation (10), the state-space equation is conducted in practice by fully considering the working characteristics and internal composition.

2.3. *Dual Unscented Transformation*

As high-order expansion terms of the transformation are ignored, the error triggered by the linearization processing may cause the system to diverge. Besides, it is difficult to obtain the derivative Jacobian matrix of the nonlinear battery system in practical application. Thus, an improved dual unscented transformation (DUT) method is introduced to calculate the random vector probability. The Sigma point set is formed in the unscented transformation on-premise of ensuring the sampling mean and covariance respectively. Applying the nonlinear transformation to each Sigma point, the sampled data point set is obtained, as shown in Equation (11).

$$\begin{cases} x_{k-1}^i = \hat{x}_{k-1} + (\sqrt{(n+k)p_{k-1}})_i, i = 1,2\cdots n \\ x_{k-1}^i = \hat{x}_{k-1} - (\sqrt{(n+k)p_{k-1}})_i, i = n+1, n+2\cdots 2n \end{cases} \tag{11}$$

In Equation (11), x_{k-1}^i is the i-th particle for the time point of $k-1$; $\hat{x}_{k-1}$ is the predicted value; n and k are coefficient parameters; p_{k-1} is the covariance for the time point of $k-1$. The DUT is conducted to realize the mathematical joint estimation of the model parameters and SOC by the functional fitting treatment, which is adaptive to different working conditions. The mathematical expression is realized for the strong nonlinear characteristics, according to which the mathematical description is revealed for different conditions. The error caused by the state-space equation linearization is eliminated from the square root value obtained by the Cholesky decomposition. After obtaining the sigma points, the quantity and variance matrices are predicted, as shown in Equation (12).

$$\begin{cases} \overline{x}_k^i = A_{K-1}\overline{x}_{k-1}^i + B_{k-1}u_{k-1} \\ \hat{x}_k = \sum_{i=0}^{2n} \omega_i^m \overline{x}_k^i \\ \overline{P}_{x,k} = \sum_{i=0}^{2n} \omega_i^c [\overline{x}_k^i - \hat{x}_k][\overline{x}_k^i - \hat{x}_k]^T + Q_k \end{cases} \quad (12)$$

In Equation (12), x_{k-1}^i is the i-th particle for the time point of $k-1$; $\hat{x}_k$ is the predicted value for the time point of k; ω_i^m is the coefficient for the $2n+1$ particles in the state prediction process; $\overline{P}_{x,k}$ is the covariance of all the $2n+1$ particles for the time point k; ω_i^c is the weighting factor for the covariance correction; Q_k is the processing noise covariance matrix. To avoid the situation of the nonpositive matrix, the square root decomposition is conducted to replace the covariance matrix in the iterative calculation. And then, the square root treatment is conducted for the covariance matrix S_k instead of P_k to participate in the iterative operation, as shown in Equation (13).

$$\begin{cases} x_{k-1} = [\hat{x}_{k-1}, \hat{x}_{k-1} + \sqrt{n+k}S_k, \hat{x}_{k-1} - \sqrt{n+k}S_k] \\ {}_k^* = qr\left\{\sqrt{\omega_i^c}(\overline{x}_{k-1}^i - \hat{x}_k), \sqrt{Q_k}\right\} \\ S_k = cholupdate\left\{S_k^*, \overline{x}_{k-1}^0 - \hat{x}_k, \omega_0^c\right\} \end{cases} \quad (13)$$

In Equation (13), x_{k-1} is the state matrix formed by three parts of the mathematical treatment for the time point of $k-1$; $\hat{x}_k$ is the predicted value for the time point of k; ω_i^c is the weighting factor for the covariance correction with an initial value of ω_0^c; Q_k is the processing noise covariance matrix; S_k is the square root of covariance matrix; the Sigma point data set x_{k-1} is obtained by the mathematical DUT treatment. The square root value is then calculated for the covariance matrix to solve the problem that the matrix cannot be decomposed because of the negative definition, as shown in Equation (14).

$$\begin{cases} \overline{y}_{k-1}^i = C_{k-1}x_{k-1} + D_{k-1}u_{k-1} \\ \hat{y}_k = \sum_{i=0}^{2n} \omega_i^m \overline{y}_{k-1}^i \end{cases} \quad (14)$$

In Equation (14), $\overline{y}_{k-1}^i$ is the observation value of the i-th particle for the time point of $k-1$; x_{k-1} is the state parameter value for the time point of $k-1$; u_{k-1} is the input parameter; C_{k-1} and D_{k-1} are the coefficient parameters for the observation function; Q_k is the processing noise covariance matrix. The resampling value is brought into the observed equation to update the time-varying variables, according to which the variance matrix at the time point k is obtained by combining the predicted value and the calculated value according to the weighting factors, as shown in Equation (15).

$$\begin{cases} S_{yy}^{*} = qr\left\{\sqrt{\omega_i^c}(\overline{y}_{k-1}^i - \hat{y}_k), \sqrt{R_k}\right\} \\ S_{yy} = cholupdate\left\{S_{yy}^{*}, \left(\overline{y}_{k-1}^0 - \hat{y}_k\right), \omega_0^c\right\} \\ P_{xy} = \sum_{i=0}^{2n} \omega_i^c [\overline{x}_{k-1}^i - \hat{x}_k][\overline{y}_{k-1}^i - \hat{y}_k]^T \end{cases} \tag{15}$$

In Equation (15), S_{yy} is the variance matrix of the output variable at the time point k; ω_i^c is weighting factors for the covariance correction with the initial value of ω_0^c; x_{k-1} is the state matrix formed by three parts of the mathematical treatment for the time point of $k-1$; $\hat{x}_k$ is the predicted value for the time point of k; Q_k is the processing noise covariance matrix; P_{xy} is the covariance matrix of the state quantity. And then, the observed state quantity of the state-space equation is introduced to calculate the Kalman gain, as shown in Equation (16).

$$K_k = {}^{P_{xy}}/\left(S_{yy}^T S_{yy}\right) \tag{16}$$

In Equation (16), K_k is the Kalman gain that has a weighting relationship between predicted and observed values; P_{xy} is the covariance matrix of state quantity; S_{yy} is the variance matrix of the output variable. Considering temperature and charge-discharge current variation influence the specific parameters of Ampere-hour (Ah) integration, the main factors are considered to describe the influences on the coulomb effect and charge-discharge efficiency. The capacity attenuation factor is proposed innovatively to characterize the coulomb and charge-discharge current efficiency effect on the available battery capacity, which is used to calibrate the available capacity for specific wide-temperature-range conditions. And then, the state matrix is updated as well as the error covariance to complete the iterative calculation, as shown in Equation (17).

$$\begin{cases} x_k = \hat{x}_k + K_k(y_k - \hat{y}_k), U_k = K_k S_{yy} \\ S_k = cholupdate\{S_{k-1}, U_k, -1\} \end{cases} \tag{17}$$

In Equation (17), x_k is the corrected state value for the time point of k; $\hat{x}_k$ is the predicted state value for the time point of k; K_k is the Kalman gain that has a weighting relationship between predicted and observed values; y_k is the measured observation value for the time point of k; $\hat{y}_k$ is the predicted observation value for the time point of k; S_k is the variance matrix of the output variable for the time point of k. In the iterative calculation procedure, the state matrix and covariance are brought into the step-to-step correction. The repeated prediction-correction treatment is conducted to update the state matrix, making the estimated state approach the measured value effectively. The available capacity is calibrated by taking the influencing factors into account, which corrects the estimation error effectively caused by the Coulomb and charge-discharge efficiency change.

The influencing calibration of the different temperature and charge-discharge current improves the estimation effect on the extreme temperature and current rate conditions. The proposed WFC-DKF algorithm realizes the accurate working state and model parameter estimation considering the low temperature and high discharging current rate influence. After analyzing the merits and demerits, the estimation accuracy is improved effectively that is adaptive to the temperature, current rate, and time-varying SOH influence. The varying capacity is analyzed for different temperature conditions and the improved Ah integral formula is constructed, as shown in Equation (18).

$$S(t) = S_T(t-1) - \eta \int_{t-1}^{t} \frac{I}{C_T} dt \tag{18}$$

In Equation (18), $S(t)$ is the SOC factor for the temperature T at the time point of t; $S_T(t-1)$ is the predicted value for the temperature T converted from the previous time point; C_T is the battery capacity considering the temperature influence of T; η is the coulomb efficiency. The available capacity change is considered according to the temperature variation, which determines the SOC conversion that varies from the previous to the present state point, improving the Ah integral performance for the low-temperature environment. As the SOH and current rate influence on the SOC estimation cannot be ignored, the adaptive integral calculation is realized by considering the parameter changes under the influence of three main factors, including temperature, charge-discharge current, and SOH. The shifting rule is further analyzed, according to which an improved composite correction factor is constructed for the Ah integral process, and the adaptive calculation formula is obtained, as shown in Equation (19).

$$S(t) = S_{(T,R)}(0) - \frac{\int_0^t I dt}{[\alpha * C(T,R)]} = S_{(T,R)}(0) - \frac{\int_0^t I dt}{F} \tag{19}$$

In Equation (19), $S_{(T,R)}(0)$ is the state factor converted to the present temperature T and current rate R from the previous time point by the combined analysis of Equation (18). During the iterative calculation process, the predicted value is updated by the assignment and conversion, which is also corrected by the real-time measured CCV value before each cyclic calculation step. $S(t)$ is the state parameter at the present temperature and current rate conditions. α is a capacity attenuation factor that varies from 0.8 to 1.0. $C(T, R)$ refers to the maximum available capacity considering the temperature and current influence. α represents the composite capacity correction factor. Using the improved Ah integral formula, the state estimation performance is optimized. Considering the environmental factors of the temperature difference and regional climate variation, the working conditions of lithium-ion batteries are affected greatly. As the average discharging current varies frequently from the power supply application and the internal parameters, the battery performance declines gradually along with the increasing charge-discharge cycles, and the composite capacity correcting factor plays a great role in improving the power supply performance.

2.4. *Weighting Factor Correction- Differential Kalman Filtering*

The noise variance is difficult to be obtained by the UKF algorithm due to the vague characteristics, so it is usually set as a fixed vacant value to simplify the calculating amount. However, the inaccurate statistical noise characteristic reduces the estimation accuracy, which even makes the calculation divergence. Consequently, the adaptive weighting factor correction is conducted that updates and transmits the noise matrix of the power supply application conditions. Automatically, the definition of the observed variable at the time point k is described by e_k in the first part of Equation (20), which is named as the absolute deviation. As the interest is mainly determined by the measurement error, the new covariance reveals error influence well, which is weighted by the previous M-time interest. After that, the new covariance is averaged to obtain the expression of H_k shown in the second part of Equation (20) named as the averaged absolute deviation. As H_k is quite big with large e_k, the root mean square (RMS) deviation (J_k) is used instead of H_k to obtain smaller Q and R with large H_k, the calculation process of which is shown in the third part of Equation (20).

$$\begin{cases} (1) e_k = \left| y_k - \hat{y}_{k|k-1} \right| \\ (2) H_k = \left(\frac{1}{M}\right) \sum_{i=k-M+1}^{k} e_k e_k^T \\ (3) J_k = \sqrt{H_k} = \sqrt{(1/M) \sum_{i=k-M+1}^{k} e_k e_k^T} \end{cases} \tag{20}$$

In Equation (20), e_k is the absolute deviation obtained by the comparison of the measured y_k and observed variable $\hat{y}_{k|k-1}$ at the time point k; H_k is averaged absolute deviation; J_k is the RMS deviation. As the estimation result is influenced greatly by the virtual window width and urged by iterative precision-correction treatment, the covariance value is predicted real-timely by the estimation principle, and M represents the window size. For the limited external measurable signal detection and the discretized digital sampling noise, the cumulative error is brought into the iterative calculation, so the updating treatment of the processing and observing noise is introduced, as shown in Equation (21).

$$(1) \begin{cases} Q_k = K_k H_k K_k^T + H_k \\ R_k = H_k - C_k P_k C_k^T \end{cases} \Rightarrow (2) \begin{cases} Q_k = K_k J_k K_k^T + J_k \\ R_k = J_k - C_k P_k C_k^T \end{cases} \tag{21}$$

In Equation (21), Q_k is the processing noise covariance matrix; R_k is the observing noise covariance matrix; H_k is averaged absolute deviation; K_k is the Kalman gain that has a weighting relationship between predicted and observed values; J_k is the RMS deviation. The observation noise is inseparable from H_k to improve the estimation accuracy along with the computational time-varying minimization treatment, and the previous three unstable innovation parts are calculated systematically as $M = 3$. Since R_k decreases gradually along with the time extension and tends to be zero eventually, it is negligible for the portion of $C_k P_k {C_k}^T$, so that the single-chip realization is conducted in a stable operating state above 3.24 V described by $S = Q_C/Q_I$ with the calculated remaining power of Q_C and the initial value of Q_I. CCV is characterized by U_L with a maximum SOC value of 1, so the ratio of Q_C to Q_I is the present SOC value and the estimation error is obtained by real-time core parameter measurement and estimation.

2.5. *Differential prediction-correction*

The available energy prediction is implemented by using the relationship between OCV and power availability, in which the Ah segmentation between temperature coefficient and the WFC-DKF algorithm is used for iterative battery state calculation. This algorithm uses minimum variance to realize the optimal co-estimation of working state and modeling parameters, which predicts variable factor values according to the recursive optimal state from the previous time point. The predicted value is then corrected by the difference between the observed and predicted values to guarantee the reliability that is suitable for both stationary and non-stationary estimation processes. Furthermore, the prediction-correction treatment is revealed, and the real-time performance evaluation is implemented conveniently. The state-space form of the scientific discretization is designed, as shown in Equation (22).

$$\begin{cases} x_k = A_{k-1} x_{k-1} + B_{k-1} u_{k-1} + w_{k-1} \\ y_k = C_k x_k + D_k u_k + v_k \end{cases} \tag{22}$$

In Equation (22), x_k is the state parameter for the time point of k; x_{k-1} is the state parameter for the time point of $k-1$; ω_i^m is the coefficient for the $2n+1$ particles in the state prediction process; $\overline{P}_{x,k}$ is the covariance of all the $2n+1$ particles for the time point of k; ω_i^c is weighting factors for the covariance correction; Q_k is the processing noise covariance matrix. Consequently, a linear relationship is constructed for the input and output variables, in which the prediction effect is obtained for the expected period and the CCV value exhibits strong nonlinearity respectively. Therefore, the specific calculating flowchart is designed to overcome the traditional limitations and restrictions, according to which the prediction accuracy is improved greatly and the calculation error is restrained effectively. And then, the required state variable is initialized as well as the covariance without repetition, as shown in Equation (23).

$$\hat{x}_{0|0} = E(x_0), P_{0|0} = Var(x_0) \tag{23}$$

In Equation (23), $\hat{x}_{0|0}$ is the estimated initial state parameter that is obtained by the expected calculation; $P_{0|0}$ is the initial covariance that is obtained by the variance treatment; x_0 is the initial state. And then, the initial state parameters are obtained by the expectation and variance calculation. The calculation structure is substituted to obtain a high-accuracy predicting effect and extend the application range of the nonlinear battery system, which has strong nonlinear changes towards the parameter variation on internal resistance, CCV, and available energy for the power supply operation that is linearized repeatedly by the first-order Taylor expansion. The state variable is updated real-timely and the prediction is investigated by Equation (24).

$$\hat{x}_{k|k-1} = A_{k-1}\hat{x}_{k-1|k-1} + B_{k-1}u_{k-1} \tag{24}$$

In Equation (24), $\hat{x}_{k|k-1}$ is the predicted state parameter from the time point $k-1$ to the time point k; u_{k-1} is the input parameter; A_{k-1} and B_{k-1} are the coefficients for the state and input correction parameters. The Taylor truncation error is produced in the linearization process, as the second-order and other high-order terms are neglected in the calculation process, which leads the prediction model to diverge in the calculation process. Moreover, the Jacobian matrix is calculated repeatedly in each cycling calculation step, which prolongs the computational time as well as the remarkable substantial resources. Consequently, the error covariance is updated with high reliability, as shown in Equation (25).

$$P_{k|k-1} = E\left[(x_k - \hat{x}_{k|k-1})(x_k - \hat{x}_{k|k-1})^T\right] = A_{k-1}P_{k-1|k-1}A_{k-1}{}^T + Q_{k-1} \tag{25}$$

In Equation (25), $P_{k|k-1}$ is the predicted error covariance from the time point $k-1$ to the time point k; x_k is the state parameter for the time point of k; $\hat{x}_{k|k-1}$ is the predicted state parameter from the time point $k-1$ to the time point k; $P_{k-1|k-1}$ is the error covariance for the time point $k-1$; A_{k-1} is the coefficient matrix for the state function; Q_{k-1} is the processing noise variance. Thus, the covariance value is optimized by the iterative calculation, in which the state and observation equations have nonlinear time-continuous characteristics. Consequently, the nonlinearity degree returns to be normal with high accuracy. Therefore, the global convergence is calculated and stretched, in which the state-space equations are used relatively and the Kalman gain matrix is obtained, as shown in Equation (26).

$$K_k = P_{k|k-1}C_k{}^T(C_kP_{k|k-1}C_k{}^T + R_k)^{-1} \tag{26}$$

In Equation (26), K_k is the Kalman gain; $P_{k|k-1}$ is the predicted error covariance from the time point $k-1$ to the time point k; C_k is the coefficient matrix for the observation function; R_k is the prediction noise variance. The proposed derivative WFC-DKF algorithm is introduced into the iterative calculation, in which an improved linearizing strategy is investigated and the state variable measurement is updated, as shown in Equation (27).

$$\hat{x}_{k|k} = \hat{x}_{k|k-1} + K_k(y_k - C_k\hat{x}_{k|k-1} - D_ku_k) \tag{27}$$

In Equation (27), $\hat{x}_{k|k}$ is the corrected state parameter for the time point of k; $\hat{x}_{k|k-1}$ is the predicted state parameter from the time point $k-1$ to the time point k; K_k is the Kalman gain; y_k is the observed parameter; C_k is the coefficient matrix for the predicted state parameters; D_k is the coefficient matrix for the input parameters. Consequently, an approximation of the probability density distribution is conducted for state variables to reinforce the stability reflected by the correcting process.

3. Experimental Analysis

3.1. *Testing Platform and Modeling Realization*

After obtaining a mathematical description of the CM-EEC model factors, the identified parameters are introduced by using the same current change in the pulse power experimental test. The estimated and referenced CCV values are compared to optimize the model structure according to the comparative results. The largest block of the structural calculation process shown at the bottom of Figure 1 is the CM-EEC model, in which the input parameters are current I, ohmic resistance R_0, polarization resistance R_p, polarization capacitor C_p, open-circuit voltage U_{OC}, closed-circuit voltage U_L, and load current I_L. In addition to the current, the input factors are internal parameters of the CM-EEC model that has a functional relationship to the SOC variation. If the terminal cut-off voltage is too low, the battery is not fully reheated and the energy release is not completed without a high adoption rate. Consequently, the cut-off voltage varies for different charge-discharge conditions, and the cut-off voltage limitation is set to be low in the discharging process. The experimental tests are also conducted at low-temperature and large current-rate conditions. The experimental platform is designed and realized, as shown in Figure 3.

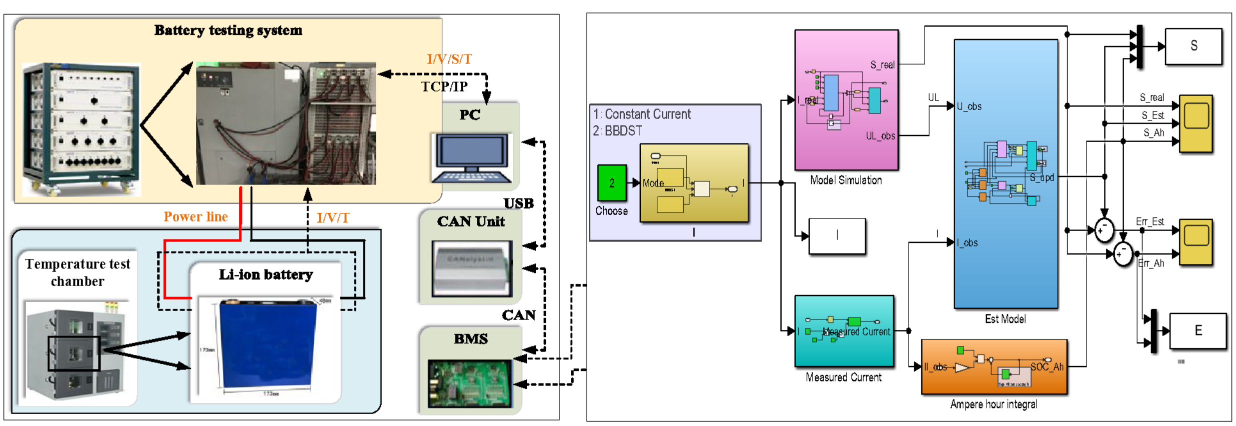

Figure 3. Lithium-ion battery characteristic experimental test platform and model construction

In Figure 3, the experimental platform structure includes the following components: (1) the battery charge-discharge tester (CT-4016-5 V100A-NTFA); (2) the independent-control temperature testing chamber; (3) the supporting experimental equipment (BTT-331C); (4) the charge-discharge measurement-control host. The main charge-discharge hybrid pulse power test is designed to verify the accuracy of the proposed CM-EEC model. The parameter identification validity is evaluated by comparing the estimated CCV value with the measured data for the same input current conditions. If the deviation is large, it indicates that parameters are not recognized with a high-precision effect or the model accuracy is defective.

3.2. *Parameter Identification and Adaptive Filtering*

The OCV value equals the stable electromotive force when the battery is shelved for more than 30 minutes, which has a close relationship with each other. In each step-by-step test, the battery is charged with the recommended C/2 current rate for 12 minutes, which is followed by a relaxation period of 40 minutes, making the battery return to a stable condition before the next cyclic test is conducted. The CCV value is measured and the experiment is continued to be repeated until the entire experimental test is completed. The curve fitting method is used to describe the polynomial relationship between OCV and SOC. In the curve fitting analysis, U_{OC} has a functional relationship to the SOC variation, which is expressed by the 6-order polynomial formula, as shown in Equation (28).

$$\begin{aligned} U_{OC} = f(S) &= P_1 \times S^6 + P_2 \times S^5 + P_3 \times S^4 + P_4 \times S^3 + P_5 \times S^2 + P_6 \times S + P_7 \\ &= 20.08 \times S^6 - 61.22 \times S^5 + 68.12 \times S^4 - 32.07 \times S^3 + 5.234 \times S^2 + 0.6794 \times S + 3.36 \end{aligned} \tag{28}$$

In Equation (28), P_1 to P_7 are coefficient parameters obtained by the least-squares curve fitting treatment, in which $f(S)$ represents the converting function of S and U_{OC}. The OCV value is 3.36 V when SOC turns to be zero. The corresponding relationship is used in the revised mathematical description of subsequent parameters to obtain the approximate capacity. The model parameters of polarization resistance and capacitance are obtained by least-squares curve fitting according to the formula defined in Equations (8) and (9). Consequently, the experimental results are obtained, as shown in Table 1.

Table 1 Discharging profile criteria under different SOC levels

S (%)	U_{OC} (V)	R_0 (Ω)	R_{p1} (Ω)	R_{p2} (Ω)	C_{p1} (F)	C_{p2} (F)
10%	3.4545	0.00148	0.00069	0.0001	17529	4495
20%	3.5367	0.00140	0.00003	0.00045	13469	27034
30%	3.5900	0.00135	0.00003	0.00038	17552	31568
40%	3.6163	0.00132	0.00034	0.00003	33144	29758
50%	3.6511	0.00131	0.00003	0.00034	20421	31815
60%	3.7366	0.00131	0.00004	0.00057	20176	23233
70%	3.8309	0.00130	0.00004	0.00064	18860	25931
80%	3.9360	0.00130	0.00004	0.00056	23504	25388
90%	4.0513	0.00130	0.00003	0.00048	19710	25491
100%	4.1840	0.00131	0.00003	0.00045	26053	28427

In Table 1, the factor influencing effect is used to describe the battery working characteristic changes of voltage, internal resistance, temperature, and self-discharge parameters. And then, the correlation feature is used for internal resistance, capacity uniformity, voltage, cycling lifespan, and output characteristics, which is used to obtain the CCV altering law towards the variation of the current rate, temperature, and other factors. Combined with experimental analysis, the in-depth influencing mechanism is discovered for the operating condition changes to obtain the characteristic variation law of the dynamic packing application. The partial least square and polynomial fitting algorithms are used to explore the mathematical representation approach suitable for different working conditions, realizing the accurate battery characteristic description. The electrical equivalent model is designed and established by the integration of the resistance-capacitance circuit. As the experimental results of R_0, R_{p1}, R_{p2}, C_{p1}, and C_{p2} reflect parameters respectively for the improved CM-EEC model, the curve fitting is conducted to obtain the parameter relationship. Subsequently, the model parameter values can be obtained according to the polynomial treatment. The evaluation parameters are introduced to analyze the estimation effect, including mean squared error (MSE) and root mean squared error (RMSE). Considering both the accuracy and the calculation complexity, the mathematical relationship between the model parameters and the SOC levels can be obtained, as shown in Equation (29).

$$\begin{cases} R_0 = 0.7082 \times S^3 - 0.5668 \times S^2 - 0.6423 \times S + 3.409; SSE: 0.001945; RMSE: 0.01801 \\ R_{p1} = 0.0011 \times S^4 - 0.0032 \times S^3 + 0.0033 \times S^2 - 0.0016 \times S + 0.0016; SSE: 4.889e-11; RMSE: 3.127e-06 \\ R_{p2} = -0.0036 \times S^3 + 0.0072 \times S^2 - 0.0044 \times S + 0.0009; SSE: 1.852e-07; RMSE: 0.0001757 \\ C_{p1} = -11970 \times S^2 + 19660 \times S + 14840; SSE: 2.249e+08; RMSE: 5668 \\ C_{p2} = -53650 \times S^2 + 68320 \times S + 8390; SSE: 3.285e+08; RMSE: 6850 \end{cases} \tag{29}$$

In Equation (29), the model parameter variation law towards the SOC variation is obtained. To realize the integral functions shown in Equations (7) and (8), the Riemann integral is approximated on the time domain with the small amplitude in division intervals, which is divided into the range of integrand functions. As long as the function is Riemann integral, it is appropriate for the Lebesgue integral as well, so these two integration methods are introduced into the iterative calculation process, as shown in Figure 4.

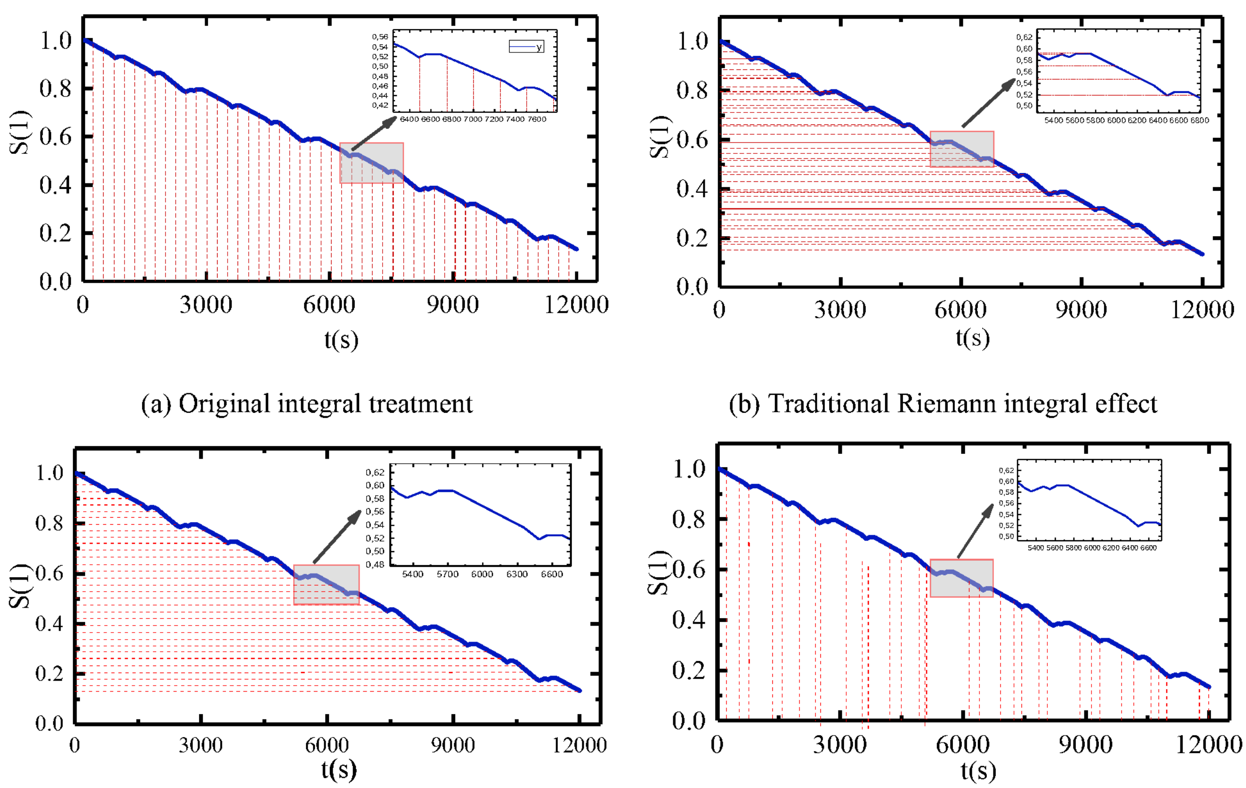

(a) Original integral treatment (b) Traditional Riemann integral effect

(c) Lebesgue integral treatment (d) Lebesgue integral application effect

Figure 4. Riemann - Lebesgue integral treatment for adaptive filtering

25

In Figure 4, the original sampling process is described in subfigure (a), which is conducted for the fixed periods in the time domain even when the sampling interval is short. And then, an iterative operation is performed at each sampling data point to update the co-estimation result of the working state and model parameters. The Riemann integral treatment is conducted corresponding to each sampling time point, as shown in subfigure (b). The dense-red dotted line depicts that mounts of iterative operations have been carried out in this period, but the estimation result converts little. Consequently, the iterative operation of sampling data points in this period is redundant and wastes a lot of processing resources. To optimize the iterative computation, the computational sampling is combined with the Lebesgue integral treatment. The schematic Lebesgue sampling diagram is shown in subfigure (c), which is dissimilar to the Riemann sampling. During the industrial application of lithium-ion batteries, so the Riemann sampling wastes more processing resources in practical engineering applications, while the Lebesgue sampling point changes obviously according to the SOC variation. The density-red dotted line represents the calculation number variation shown in subfigure (d). The denser the dotted line, the more the calculation number is. The calculation number reduces in a stage when the SOC changes slowly. When the SOC change is insignificant in a period, the iterative operation is an iterative operating strategy in the SOC estimation process that greatly reduces the processing occupation time requirements.

3.3. *Multiple Current-rate Characteristic Tests*

The experiments adopt mixed pulse power performance of the battery charge-discharge test, recording the OCV-SOC change for the analog circuits and current. And then, the state-space equation of the CM-EEC model is used to obtain the internal model parameters. The pulse power test is conducted in the charging process to obtain the CCV value for various current conditions. The OCV-SOC relationship curve is obtained by experimental results, in which the theoretical value of various model parameters is obtained by the characteristic description equations. The charging mode of constant-current (CC) to constant-voltage (CV) is conducted by taking 4.20 V as the terminal charging voltage. The nominal charging current rate is set to be 0.20 C to 1.20 C in the experiment to obtain the CV variation curve in the charging process, as shown in Figure 5.

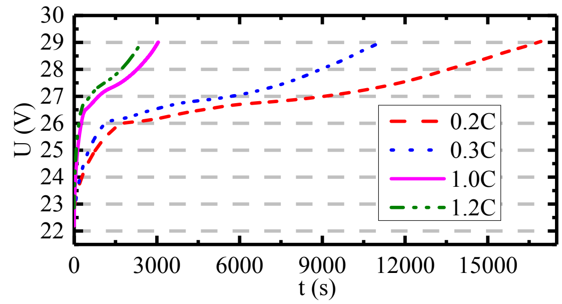

(a) Charging voltage-current characteristics

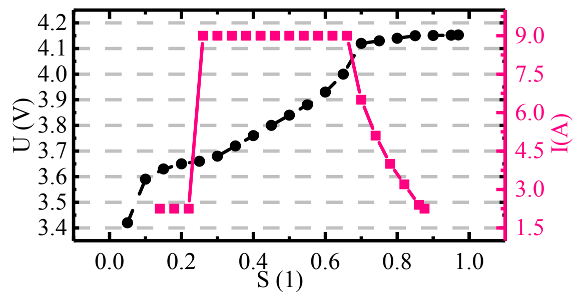

(b) Different multiplying charge power stages

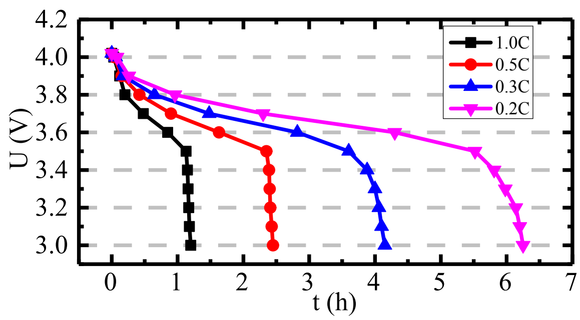

(c) Cell OCV for different current rates

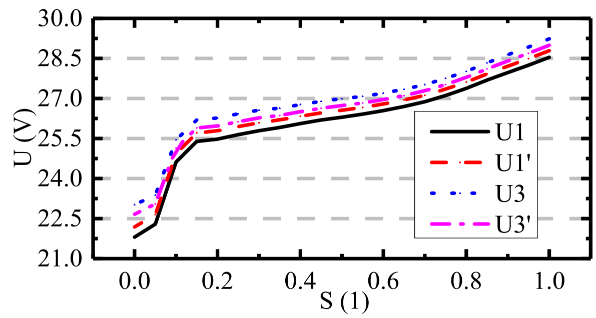

(d) OCV variation for battery packs

Figure 5 Experimental voltage response characteristics for battery cells and packs

In Figure 5, the discharging experiment is carried on the lithium-ion batteries by CC treatment using different magnifying current rates, and the relationship between voltage and time is obtained at each discharging current rate. As can be known from the observation curve, the available capacity is smaller with a higher discharge current rate. When the SOC continues to decline, the bigger the current rate, the faster the discharge speed is. The OCV-SOC calibration is conducted as an intermittent discharge result. For each SOC=0.1 variation, the battery is shelved for 45 minutes before the next experimental test. The battery CCV value in this stage is used as OCV value. And finally, the relationship curve is obtained between OCV and SOC through the experimental tests shown in Figure 5 (c) and (d). In Figure 5 (d), U1 is the voltage value at the end of pulse discharge; U1' is the voltage value after the voltage rises rapidly for the pulse discharge; U3 is the voltage value at the end of pulse charging; U3' is the voltage value after the voltage rises rapidly for the end of pulse charging. In the same SOC conditions, the battery voltage soars significantly along with the discharge current rate variation. Due to constraints on all aspects of time-varying working conditions, the SOC variation is between 0.8 and 0.2, according to which the CCV value is stable relatively. When the current values continue to increase or decrease, the line moves closer to the terminal levels gradually, which is one of the essential characteristics of the charge-discharge process.

3.4. *Complex Time-varying Voltage Traction*

All voltage characteristics are extracted from the original data as well as the CCV change in the pulse power test. The available capacity is calibrated at different SOC conditions and the OCV switching law is also obtained, as shown in Figure 6.

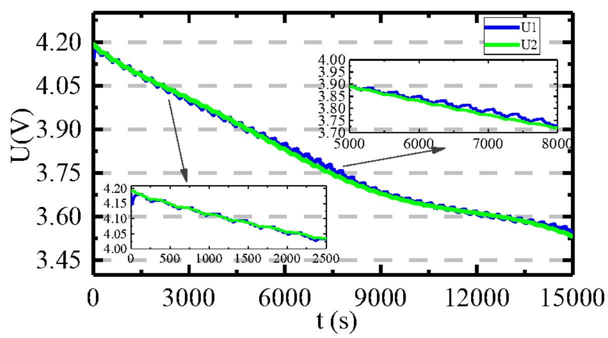

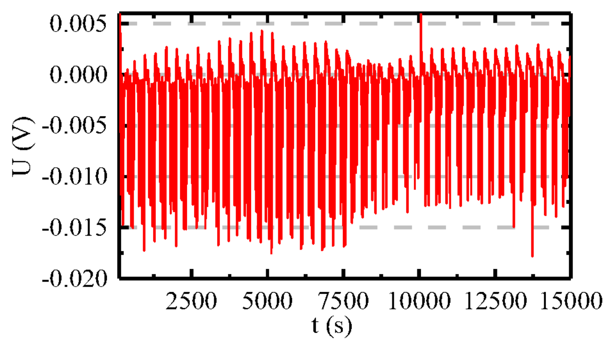

(a) OCV recognition results

(b) CCV traction error variation curve

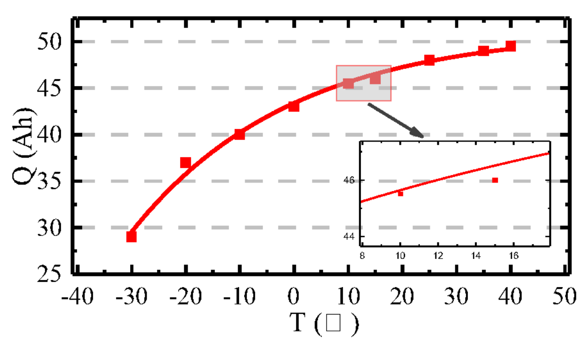

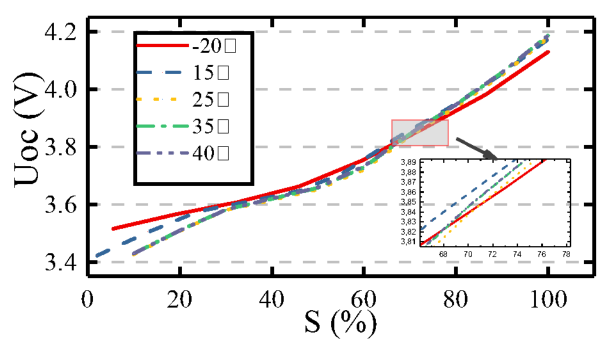

(c) Capacity variation towards temperature change (d) OCV variation at different temperature conditions

Figure 6. Experimental voltage response to the complex time-varying current variation

In Figure 6, the CCV change in the pulse power test is depicted as illustrated in subgraph (a) and (b); the available capacity is calibrated at different SOC conditions, according to which the capacity changing curve towards the temperature variation is shown in subgraph (c); the OCV switching law is obtained through an experimental test corresponding to different temperature conditions, as shown in subgraph (d). The battery CCV value increases gradually after a one-hour shelved period at the end of each CC discharge treatment. The internal chemical reaction is struck as a basic SOB considering the thermal effect, so the CCV value at this time point equals the OCV value. Consequently, the OCV-SOC relationship is obtained. As the result is much the same as the OCV fitting curve, several useful data segments are extracted from the overall processing data before the parameter identification is performed.

3.5. *Closed-Circuit Voltage Prediction Effect*

The model output voltage responds well to battery current variation, and the maximum error is 0.165 V. As the terminal voltage is 4.20 V for the charging CCV of lithium-ion batteries, the model accuracy is better than 96.07%, which is the same with battery experimental characteristics under charging conditions. And then, the operating energy equilibrium index is analyzed separately for the CC discharge process. The CCV measurement scheme is designed as follows. S1: The battery is charged with 1/3 C to 4.15 V and turns to be CC charging until the current rate is lower than 0.05 C. S2: The battery is then shelved for 30 minutes. S3: The battery is discharged at a current rate of 0.2 C for 5.00% of the rated capacity and the CCV value is measured in this period until the charging is stopped. S4: The battery is shelved again for 30 minutes and the corresponding CCV value is recorded. S5: The procedure of S1 to S4 is repeated to carry out a cyclic pulse power test, and the CCV value is measured when SOC equals 0.95, 0.90, 0.85, ⋯, and 0.05 in sequence. S6: The procedure of S1 to S5 is repeated to obtain the OCV value under the discharge current rate conditions of 0.40 C, 0.50 C, and 0.80 C. The comparative analysis is conducted by using the established platform and experimental results, as shown in Figure 7.

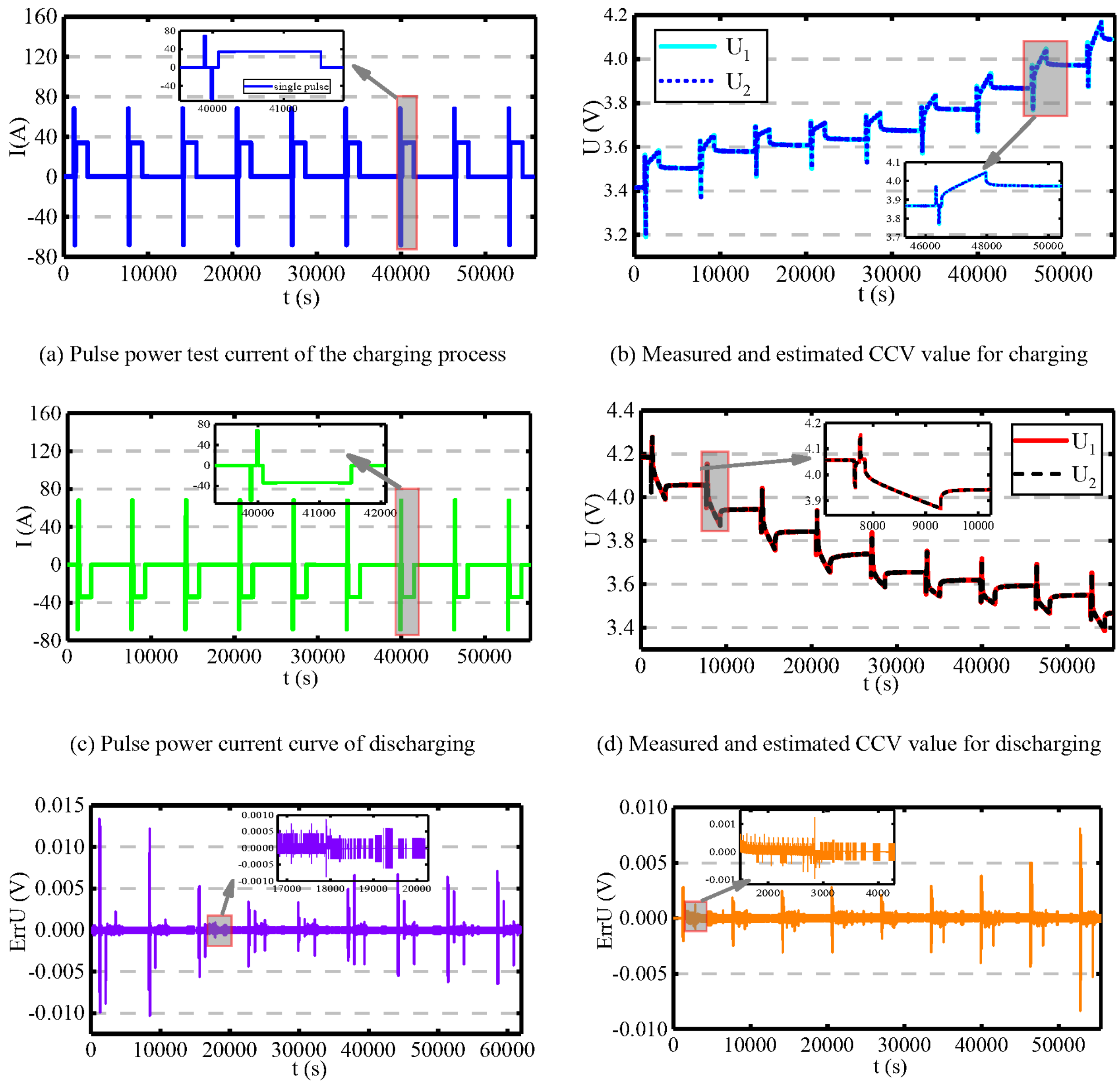

(a) Pulse power test current of the charging process

(b) Measured and estimated CCV value for charging

(c) Pulse power current curve of discharging

(d) Measured and estimated CCV value for discharging

(e) Voltage estimation error of the pulse charging

(f) Voltage estimation error of the pulse discharging

Figure 7. The hybrid pulse power test results in the main charge-discharge maintenance process

In Figure 7, the voltage error curves are described in the subgraph (e) and (f), in which the maximum estimation error is 0.015 V until the CCV value reaches 4.20 V for the pulse-power charging process. Meanwhile, the maximum recognition error is 0.01 V in the pulse-power discharging process. The CCV change of the battery cell is obtained for different discharging current rates, in which the working voltage is extremely stricken in the same SOC level. When the discharging current rate is large, the manipulating voltage is small for the same SOC level. The overall high current rate curves are below low current rate ones, which are similar to the charging voltage curves. The CCV value changes rapidly at both ends of the variation curve, and the developing trend at the intermediate stage is minor. The CCV change caused by each 0.10 C current rate variation is 5 to 10 mV.

3.6. *Packing SOC Estimation Analysis for Phased Working Conditions*

To verify the effect of packing SOC estimation, the phased working condition experimental test procedure is designed and realized for the packing lithium-ion batteries. In the experimental tests, the current varies along with the time extension, so that the modeling effect can be verified effectively. Combined with experimental tests of different discharge current rates, the SOC estimation performance is analyzed under complex working conditions along with the CCV tracking effect analysis for the lithium-ion battery packs. The experimental SOC estimation and CCV tracking curve towards the composite current rate variation are obtained, as shown in Figure 8.

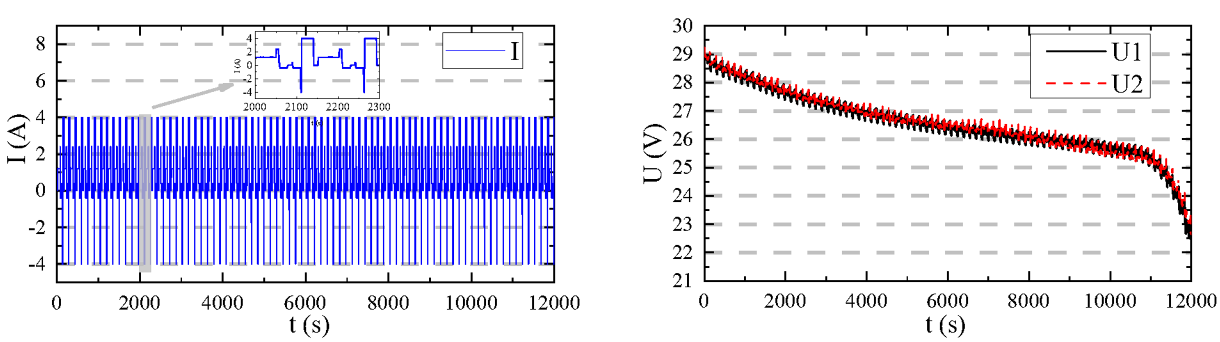

(a) Phased current rate profile

(b) CCV and SOC profiles

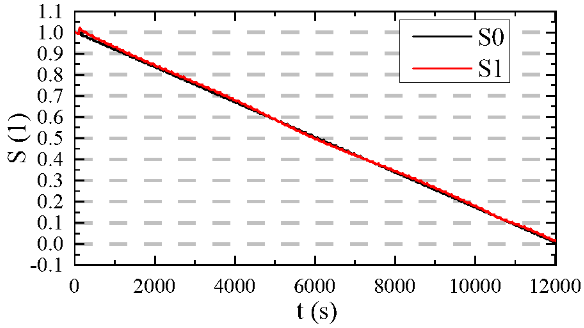

(c) Estimated result comparison

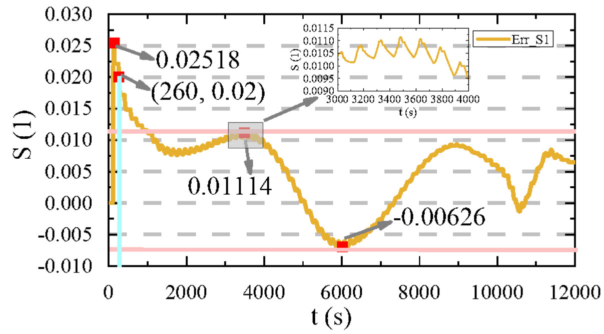

(d) Estimated error comparison

Figure 8. The index curves of phased working condition experiments

In Figure 8, the current variation of the packing pulse-current charge-discharge is shown in subgraph (a) and the whole experimental test is composed of cycling multiple current variation process; the CCV changing curve and tracking effect towards the current variation are described as shown in subgraph (b); the SOC estimation effect is shown in subgraph (c) by taking S0 as the measured value and S1 as the estimated value; the comparative SOC estimation error is described as shown in subgraph (d). As can be known from the experimental results, the SOC estimation has manifest oscillation under drastic current change conditions. The maximum CCV tracking error is 0.32 V with an error percentage of 1.07%. The maximum SOC estimation error for packing lithium-ion batteries is 1.114% for the long-term experimental tests with the MAE value of 0.00481 and RMSE value of 5.44085E-5. The SOC estimation curve can track the measured variation law within 260 s when the estimation results fall in the 2.00% tracking error range. In contrast, the improved algorithm has a robustness effect and high accuracy, which satisfies the high-performance requirement. The influencing factors of the feasible charge-discharge treatment mainly include voltage, current, and temperature, so the battery performance is affected by the different order duration of various stages greatly.

4. Conclusion

An improved covariance matching - electrical equivalent circuit (CM-EEC) modeling method is proposed by considering complex working condition influences, which reflects the battery working characteristics effectively when the current rate and temperature changes. An improved weighting factor correction - differential Kalman filtering (WFC-DKF) model is constructed for the iterative calculation, in which the adaptive covariance matching treatment is investigated to update and transmit the noise matrix for high-power energy supply conditions. Combined with influencing factor analysis and correction strategy design, the inter-unit inconsistency effect is reduced effectively. The battery transient characteristics are adapted effectively by considering the current rate and temperature variation influence, which simulates the charge-discharge process accurately by considering the OCV change contributed to the current accumulation. The maximum error of the CCV traction is obtained with an error percentage of 1.80%. The maximum SOC estimation error for packing lithium-ion batteries is 1.114% for the long-term experimental tests with the MAE value of 0.00481 and RMSE value of 5.44085E-5. Verified by the complex time-varying working conditions, the model is adaptive to both the long-term and transient energy supply working conditions, including the fast and slow current changing processes. Thus, the improved CM-EEC modeling and WFC-DKF iterative calculation methods provide a useful reference for the working state monitoring of packing lithium-ion batteries in the long-term application and transient energy supply processes.

Data availability

The authors declare that the main data supporting the findings of this study are available within the article and its supporting information files. Extra data are available from the corresponding authors on reasonable request.

https://www.researchgate.net/project/Battery-life-test

Acknowledgments

The work was supported by the National Natural Science Foundation of China (No. 62173281, 61801407), Sichuan science and technology program (No. 2019YFG0427), China Scholarship Council (No. 201908515099), and Fund of Robot Technology Used for Special Environment Key Laboratory of Sichuan Province (No. 18kftk03).

References

1. Zhang, Z.Y., et al., *Active cell balancing of lithium-ion battery pack based on average state of charge.* International Journal Of Energy Research, 2020. **44**(4): p. 2535-2548.
2. Pradeeswari, K., et al., *Study on the electrochemical performance of ZnO nanoparticles synthesized via non-aqueous sol-gel route for supercapacitor applications.* Materials Research Express, 2019. **6**(10).
3. Pradeeswari, K., et al., *Effect of cerium on electrochemical properties of V2O5 nanoparticles synthesized via non-aqueous sol-gel technique.* Ionics, 2020. **26**(2): p. 905-912.
4. Li, D., et al., *Battery Fault Diagnosis for Electric Vehicles Based on Voltage Abnormality by Combining the Long Short-Term Memory Neural Network and the Equivalent Circuit Model.* Ieee Transactions on Power Electronics, 2021. **36**(2): p. 1303-1315.
5. Bian, X.L., et al., *A Two-Step Parameter Optimization Method for Low-Order Model-Based State-of-Charge Estimation.* Ieee Transactions on Transportation Electrification, 2021. **7**(2): p. 399-409.
6. Oyewole, I., et al., *Optimal Discretization Approach to the Enhanced Single-Particle Model for Li-Ion Batteries.* Ieee Transactions on Transportation Electrification, 2021. **7**(2): p. 369-381.
7. Wang, Q.S., et al., *A Novel Consistency Evaluation Method for Series-Connected Battery Systems Based on Real-World Operation Data.* Ieee Transactions on Transportation Electrification, 2021. **7**(2): p. 437-451.
8. Shateri, N., et al., *Lithium-Sulfur Cell State of Charge Estimation Using a Classification Technique.* Ieee Transactions on Vehicular Technology, 2021. **70**(1): p. 212-224.
9. Shrivastava, P., et al., *Combined State of Charge and State of Energy Estimation of Lithium-Ion Battery Using Dual Forgetting Factor-Based Adaptive Extended Kalman Filter for Electric Vehicle Applications.* Ieee Transactions on Vehicular Technology, 2021. **70**(2): p. 1200-1215.
10. Sethia, G., et al., *Strict Lyapunov super twisting observer design for state of charge prediction of lithium-ion batteries.* Iet Renewable Power Generation, 2021. **15**(2): p. 424-435.
11. Han, W.J., et al., *Estimation of Cell SOC Evolution and System Performance in Module-Based Battery Charge Equalization Systems.* Ieee Transactions on Smart Grid, 2019. **10**(5): p. 4717-4728.
12. Xu, Y.D., et al., *State of charge estimation for lithium-ion batteries based on adaptive dual Kalman filter.* Applied Mathematical Modelling, 2020. **77**: p. 1255-1272.
13. Lotfi, F., et al., *A switched SDRE filter for state of charge estimation of lithium-ion batteries.* International Journal of Electrical Power & Energy Systems, 2020. **117**.
14. Lai, X., et al., *Parameter sensitivity analysis and simplification of equivalent circuit model for the state of charge of lithium-ion batteries.* Electrochimica Acta, 2020. **330**.
15. Bian, C., et al., *State-of-charge sequence estimation of lithium-ion battery based on bidirectional long short-term*

memory encoder-decoder architecture. Journal of Power Sources, 2020. **449**.

16. Yang, L., et al., *Supervisory long-term prediction of state of available power for lithium-ion batteries in electric vehicles.* Applied Energy, 2020. **257**: p. 1-14.
17. Li, S., et al., *A novel model predictive control scheme based observer for working conditions and reconditioning monitoring of Zinc-Nickel single flow batteries.* Journal of Power Sources, 2020. **445**.
18. Hou, J., Y. Yang, and T. Gao, *A normal-gamma-based adaptive dual unscented Kalman filter for battery parameters and state-of-charge estimation with heavy-tailed measurement noise.* International Journal of Energy Research, 2020.
19. Hou, J. and Z.Y. Song, *A hierarchical energy management strategy for hybrid energy storage via vehicle-to-cloud connectivity.* Applied Energy, 2020. **257**.
20. Jiang, Q.Q., et al., *Black phosphorus with superior lithium ion batteries performance directly synthesized by the efficient thermal-vaporization method.* Electrochimica Acta, 2018. **263**: p. 272-276.
21. Tan, T., et al., *An Approach to Estimate Lithium-Ion Battery State of Charge Based on Adaptive Lyapunov Super Twisting Observer.* Ieee Transactions on Circuits And Systems I-Regular Papers, 2021. **68**(3): p. 1354-1365.
22. Lee, C., et al., *Capacity-Fading Behavior Analysis for Early Detection of Unhealthy Li-Ion Batteries.* Ieee Transactions on Industrial Electronics, 2021. **68**(3): p. 2659-2666.
23. Liu, K.L., et al., *A Data-Driven Approach With Uncertainty Quantification for Predicting Future Capacities and Remaining Useful Life of Lithium-ion Battery.* Ieee Transactions on Industrial Electronics, 2021. **68**(4): p. 3170-3180.
24. Wang, C., Y.Y. Yang, and P.Z. Zhou, *Towards Efficient Scheduling of Federated Mobile Devices Under Computational and Statistical Heterogeneity.* Ieee Transactions on Parallel And Distributed Systems, 2021. **32**(2): p. 394-410.
25. Dai, H.D., et al., *A Novel Estimation Method for the State of Health of Lithium-Ion Battery Using Prior Knowledge-Based Neural Network and Markov Chain.* Ieee Transactions on Industrial Electronics, 2019. **66**(10): p. 7706-7716.
26. Zhou, W., et al., *A novel interval-based approach for quantifying practical parameter identifiability of a lithium-ion battery model.* International Journal Of Energy Research, 2020. **44**(5): p. 3558-3573.
27. Xie, Y., et al., *Novel Mesoscale Electrothermal Modeling for Lithium-Ion Batteries.* Ieee Transactions on Power Electronics, 2020. **35**(3): p. 2595-2614.
28. Xie, Y., et al., *An improved resistance-based thermal model for a pouch lithium-ion battery considering heat generation of posts.* Applied Thermal Engineering, 2020. **164**.
29. Bi, Y.L. and S.Y. Choe, *An adaptive sigma-point Kalman filter with state equality constraints for online state-of-charge estimation of a Li(NiMnCo)O-2/Carbon battery using a reduced-order electrochemical model.* Applied Energy, 2020. **258**.
30. Banguero, E., et al., *Diagnosis of a battery energy storage system based on principal component analysis.* Renewable Energy, 2020. **146**: p. 2438-2449.
31. Wang, Y.F., et al., *Black Phosphorous Quantum Dots Sandwiched Organic Solar Cells.* Small, 2019. **15**(47).
32. Wang, Y.J., et al., *A fractional-order model-based state estimation approach for lithium-ion battery and ultra-capacitor hybrid power source system considering load trajectory.* Journal Of Power Sources, 2020. **449**: p. 1-12.
33. Wang, S.L., et al., *A novel power state evaluation method for the lithium battery packs based on the improved external measurable parameter coupling model.* Journal of Cleaner Production, 2020. **242**(118506): p. 1-13.
34. Wang, S.L., et al., *A novel safety assurance method based on the compound equivalent modeling and iterate reduce particle-adaptive Kalman filtering for the unmanned aerial vehicle lithium ion batteries.* Energy Science &

Engineering, 2020.
35. Lang, P., et al., *Recent Advances and Prospects of Metal-Based Catalysts for Oxygen Reduction Reaction.* Energy Technology, 2020. **8**(3).
36. Wang, D., et al., *Battery prognostics at different operating conditions.* Measurement, 2020. **151**.
37. Xiong, R., et al., *Online Fault Diagnosis of External Short Circuit for Lithium-Ion Battery Pack.* Ieee Transactions on Industrial Electronics, 2020. **67**(2): p. 1081-1091.
38. Liu, L.S., et al., *Comparative study on substitute triggering approaches for internal short circuit in lithium-ion batteries.* Applied Energy, 2020. **259**.
39. Gan, Y.H., et al., *Development of thermal equivalent circuit model of heat pipe-based thermal management system for a battery module with cylindrical cells.* Applied Thermal Engineering, 2020. **164**.
40. Galatro, D., et al., *Challenges in data-based degradation models for lithium-ion batteries.* International Journal of Energy Research, 2020.
41. Cheng, F., Y. Hu, and L.X. Zhao, *Analysis of weak solutions for the phase-field model for lithium-ion batteries.* Applied Mathematical Modelling, 2020. **78**: p. 185-199.
42. Chen, X.P., et al., *Dynamic behavior and modeling of prismatic lithium-ion battery.* International Journal of Energy Research, 2020.
43. Xue, Z.W., et al., *Remaining useful life prediction of lithium-ion batteries with adaptive unscented kalman filter and optimized support vector regression.* Neurocomputing, 2020. **376**: p. 95-102.
44. Xiong, R., et al., *A set membership theory based parameter and state of charge co-estimation method for all-climate batteries.* Journal Of Cleaner Production, 2020. **249**: p. 1-14.
45. Zhou, Y.P., M.H. Huang, and M. Pecht, *Remaining useful life estimation of lithium-ion cells based on k-nearest neighbor regression with differential evolution optimization.* Journal Of Cleaner Production, 2020. **249**: p. 1-12.
46. Gan, C.Q., et al., *Research progress of two-dimensional layered and related derived materials for nitrogen reduction reaction.* Sustainable Energy & Fuels, 2021. **5**(13): p. 3260-3277.
47. Beelen, H., H.J. Bergveld, and M.C.F. Donkers, *Joint Estimation of Battery Parameters and State of Charge Using an Extended Kalman Filter: A Single-Parameter Tuning Approach.* Ieee Transactions on Control Systems Technology, 2021. **29**(3): p. 1087-1101.
48. Tian, N., et al., *Nonlinear Double-Capacitor Model for Rechargeable Batteries: Modeling, Identification, and Validation.* Ieee Transactions on Control Systems Technology, 2021. **29**(1): p. 370-384.
49. Sihvo, J., T. Roinila, and D.I. Stroe, *Novel Fitting Algorithm for Parametrization of Equivalent Circuit Model of Li-Ion Battery From Broadband Impedance Measurements.* Ieee Transactions on Industrial Electronics, 2021. **68**(6): p. 4916-4926.
50. Li, Y., et al., *Constrained Ensemble Kalman Filter for Distributed Electrochemical State Estimation of Lithium-Ion Batteries.* Ieee Transactions on Industrial Informatics, 2021. **17**(1): p. 240-250.
51. Tian, N., H.Z. Fang, and Y.B. Wang, *Real-Time Optimal Lithium-Ion Battery Charging Based on Explicit Model Predictive Control.* Ieee Transactions on Industrial Informatics, 2021. **17**(2): p. 1318-1330.
52. Fan, X.Y., et al., *Simplified Battery Pack Modeling Considering Inconsistency and Evolution of Current Distribution.* Ieee Transactions on Intelligent Transportation Systems, 2021. **22**(1): p. 630-639.
53. Sun, B.X., et al., *Study of Parameters Identification Method of Li-Ion Battery Model for EV Power Profile Based on Transient Characteristics Data.* Ieee Transactions on Intelligent Transportation Systems, 2021. **22**(1): p. 661-672.
54. Tian, J.P., et al., *Online simultaneous identification of parameters and order of a fractional order battery model.* Journal Of Cleaner Production, 2020. **247**: p. 1-14.
55. Tagade, P., et al., *Deep Gaussian process regression for lithium-ion battery health prognosis and degradation*

mode diagnosis. Journal Of Power Sources, 2020. **445**: p. 1-14.

56. Ng, B., et al., *Non-destructive parameter extraction for a reduced order lumped electrochemical-thermal model for simulating Li-ion full-cells.* Journal of Power Sources, 2020. **445**.

Competing interests

The authors declare no competing interests.

Additional information

Supplementary information is available for this paper on the website.

https://www.researchgate.net/lab/DTlab-Shunli-Wang

Correspondence and requests for materials can be addressed to the corresponding authors.